Probing vorticity structure in heavy-ion collisions by local Λ polarization

Xiao-Liang Xia, Hui Li, Zebo Tang, and Qun Wang
Department of Modern Physics, University of Science and Technology of China, Hefei, Anhui 230026, China

(Received 4 March 2018; published 8 August 2018)

We study the local structure of the vorticity field and the Λ polarization in Au+Au collisions in the energy range $\sqrt{s_{\rm NN}} = 7.7$–200 GeV and Pb+Pb collisions at $\sqrt{s_{\rm NN}} = 2760$ GeV using a multiphase transport model. We focus on the vorticity field arising from the nonuniform expansion of the fireball, which gives the circular structure of the transverse vorticity $\boldsymbol{\omega}_\perp = (\omega_x, \omega_y)$ around the z direction as well as the quadrupole pattern of the longitudinal vorticity ω_z in the transverse plane. As a consequence, the three components of the polarization vector $\mathbf{P} = (P_x, P_y, P_z)$ for Λ hyperons show harmonic behaviors as $\mathrm{sgn}(Y)\sin\phi_p$, $-\mathrm{sgn}(Y)\cos\phi_p$, and $-\sin(2\phi_p)$, where ϕ_p and Y are the azimuthal angle and rapidity in momentum space. These patterns of the local Λ polarization are expected to be tested in future experiments.

DOI: 10.1103/PhysRevC.98.024905

I. INTRODUCTION

In noncentral heavy-ion collisions, huge orbital angular momenta and vorticity fields are produced in strongly coupled quark gluon plasma (sQGP). They can lead to the hadron polarization and spin alignment through spin-orbit couplings [1–5] or spin-vorticity couplings [6–9], see Refs. [10–12] for recent reviews. The vorticity-related effects also include some chiral transport phenomena such as the chiral vortical effect [13] and the chiral vortical wave [14] as well as a change of the QCD phase diagram [15–18].

The study of the global polarization was initially motivated by the fact that a huge orbital angular momentum (OAM) is produced in noncentral heavy-ion collisions as shown in Fig. 1(a). Although such an OAM does not make the sQGP rotating as a rigid body, it can manifest itself as an initial longitudinal shear flow $\partial_x v_z > 0$ in the fireball as shown in Fig. 1(b). Then a vorticity field is generated and points to the direction of the global OAM ($-y$ direction) in average and leads to the global polarization of hadrons along the same direction.

Recently, the global polarization of Λ hyperons in relativistic heavy-ion collisions has been measured by the STAR Collaboration [19] through their weak decays. The average vorticity of the sQGP has been extracted to be of order $\omega \sim 10^{21}$ s^{-1}, the highest that has ever been found in nature. One feature of the global polarization is that it decreases with collision energies in the range of 7.7–200 GeV [19]. Several different models have been used to calculate the vorticity-induced global polarization of Λ hyperons, including hydrodynamics [20,21], a multiphase transport (AMPT) model with an assumption of local thermodynamical equilibrium [22,23], AMPT model with the chiral kinetic equation [24], and the quark-gluon-string model (QGSM) with anomalous mechanism [25]. The results of these models show the same energy dependence for the global Λ polarization, which agree with experimental data. For other studies on vorticity fields or polarizations, see Refs. [26–39].

In a previous paper by some of us [22], we pointed out that the global polarization is related to the fireball's tilted shape in the reaction plane. Due to the faster longitudinal expansion at higher energies, the fireball or the matter distribution shows a less tilted shape in midrapidity, and thus the net vorticity and the global polarization are almost vanishing. Such an energy dependence of the tilted shape can also be seen by the rapidity slope of the directed flow $dv_1/d\eta$ [11].

The global polarization is an average effect over the whole volume of the fireball within the detector's acceptance, so it reflects the global or net vorticity, which is along the global OAM. However, the local vorticity field has much richer information than the global one. In the numerical simulations [22,23,31–35], it is observed that ω_y shows a quadrupole pattern in the reaction plane (xz plane): ω_y is negative and positive in the regions $xz > 0$ and $xz < 0$, respectively. This novel structure is mainly due to the fact that the transverse velocity $|v_x|$ decreases with rapidity or $\partial|v_x|/\partial|z| < 0$ [33]. In addition to the pattern of ω_y, a similar quadrupole structure of ω_z also exists in the transverse plane [11,40,41] since the transverse velocity $\mathbf{v}_\perp = (v_x, v_y)$ is not exactly along the radial direction $\mathbf{e}_r$ due to the fireball's elliptic shape in the transverse plane.

In this paper, we give a systematic analysis of the patterns of the fluid velocity and vorticity in the fireball produced in heavy-ion collisions. We find that all components, ω_x, ω_y, and ω_z, have quadrupole patterns in the yz, xz, and xy plane, respectively. These quadrupole patterns all arise from the fireball expansion not related to the OAM. In order to probe the quadrupole pattern of the vorticity field, one can separate the whole momentum space into different regions and measure the average Λ polarization in each region separately. Through the numerical simulation with the AMPT model, we find that the quadrupole patterns of vorticity fields can lead to a sizable local Λ polarization and are expected to be measured in future experiments.

This paper is organized as follows. We first give a brief introduction to the polarization induced by vorticity in Sec. II.

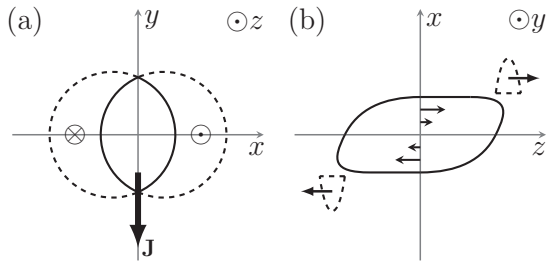

FIG. 1. Illustration of noncentral heavy-ion collisions in (a) the transverse plane and (b) the reaction plane. Two nuclei at ($x = \pm b/2,\ y = 0$) move along $\pm z$ direction, respectively. The global OAM and the net vorticity is along $-y$ direction.

Then we discuss in Sec. III how the fluid velocity and vorticity are distributed in the fireball. The local vorticity structure can be probed by the local Λ polarization. In Sec. IV, we present the numerical results for the local Λ polarization by the AMPT model. The purpose of our numerical calculation is to give some typical features of the local Λ polarization, which can be used to probe the local vorticity distribution in future experiments. A summary of results is given in the final section.

II. BASICS ON VORTICITY, SPIN, AND POLARIZATION

In this section, we give a brief introduction to the polarization induced by vorticity in a hydrodynamical system. In a nonrelativistic fluid, the vorticity can be used to characterize the local rotation of the fluid,

$$\boldsymbol{\omega} = \tfrac{1}{2}\nabla \times \mathbf{v}, \tag{1}$$

where $\mathbf{v}$ is the fluid velocity as a function of space-time. Particles with spin degrees of freedom in the vortical fluid are expected to be polarized in alignment with the vorticity. In local thermodynamical equilibrium, the ensemble average of the spin vector for the spin-1/2 particle is given by $\mathbf{S} = \mathrm{tr}(\rho\widehat{\mathbf{S}})$, where $\widehat{\mathbf{S}} = \boldsymbol{\sigma}/2$ is the spin operator with $\boldsymbol{\sigma}$ being Pauli matrices and $\rho \sim \exp(\widehat{\mathbf{S}}\cdot\boldsymbol{\omega}/T)$ is the spin density matrix with the temperature T. One can obtain $\mathbf{S}$ as

$$\mathbf{S} = \frac{1}{2}\tanh\left(\frac{\omega}{T}\right)\hat{\boldsymbol{\omega}} \simeq \frac{\boldsymbol{\omega}}{4T}, \tag{2}$$

where $\hat{\boldsymbol{\omega}} = \boldsymbol{\omega}/|\boldsymbol{\omega}|$ is the direction of $\boldsymbol{\omega}$. The polarization vector for the spin-1/2 particle is defined as

$$\mathbf{P} \equiv 2\mathbf{S} = \tanh\left(\frac{\omega}{T}\right)\hat{\boldsymbol{\omega}} \simeq \frac{\boldsymbol{\omega}}{2T}, \tag{3}$$

where the factor 2 is introduced to normalize the polarization magnitude to unity.

Since the high-energy heavy-ion collision is a relativistic system, the above equations should be generalized to the relativistic ones. As argued in Refs. [6,7], the quantity that is related to the polarization is the thermal vorticity tensor $\varpi_{\mu\nu}$ defined by

$$\varpi_{\mu\nu} = \tfrac{1}{2}(\partial_\nu\beta_\mu - \partial_\mu\beta_\nu), \tag{4}$$

where $\beta^\mu = u^\mu/T$ with $u^\mu = \gamma(1,\mathbf{v})$ being the fluid four-velocity and $\gamma = 1/\sqrt{1-\mathbf{v}^2}$ the Lorentz factor. The vorticity tensor $\varpi_{\mu\nu}$ can be decomposed into two groups of components as

$$\boldsymbol{\varpi}_T = (\varpi_{0x},\varpi_{0y},\varpi_{0z}) = \frac{1}{2}\left[\nabla\left(\frac{\gamma}{T}\right) + \partial_t\left(\frac{\gamma\mathbf{v}}{T}\right)\right], \tag{5}$$

$$\boldsymbol{\varpi}_S = (\varpi_{yz},\varpi_{zx},\varpi_{xy}) = \frac{1}{2}\nabla\left(\frac{\gamma\mathbf{v}}{T}\right). \tag{6}$$

In the Boltzmann limit and linear order of $\varpi_{\mu\nu}$, the spin vector is given by [22]

$$\mathbf{S}(x,p) = \frac{1}{4m}(E_p\boldsymbol{\varpi}_S + \mathbf{p}\times\boldsymbol{\varpi}_T). \tag{7}$$

where E_p, $\mathbf{p}$, and m are the energy, momentum, and mass of the particle. In the numerical simulations, $\mathbf{S}$ in Eq. (7) is usually calculated in the center of mass frame of A+A collisions, while in experiments the polarization is measured in the Λ's rest frame by the angular distribution of the proton in Λ's weak decay. To obtain the spin vector $\mathbf{S}^*$ in the Λ's rest frame from $\mathbf{S}$ in the calculational frame, one uses the Lorentz transformation

$$\mathbf{S}^* = \mathbf{S} - \frac{\mathbf{p}\cdot\mathbf{S}}{E_p(m+E_p)}\mathbf{p}. \tag{8}$$

In this case, the Λ polarization vector is given by

$$\mathbf{P} = 2\mathbf{S}^*, \tag{9}$$

corresponding to the nonrelativistic one in Eq. (3).

Both Eqs. (2), (3) and their relativistic generalizations, Eqs. (7)–(9), relate the polarization to the vorticity field where and when a particle such as Λ is formed at one space-time point. Therefore the local structure of the vorticity can be probed by measuring the local Λ polarization. This is the general idea we will follow throughout this study.

III. FLUID VELOCITY AND VORTICITY FIELDS AND POLARIZATION DISTRIBUTIONS

We now discuss the fluid velocity and vorticity fields. In order to give an intuitive picture, our discussion is based on Eqs. (1)–(3) using nonrelativistic fields $\mathbf{v}$ and $\boldsymbol{\omega}$, while the numerical calculations for polarizations in the next section are based on relativistic quantities in Eqs. (4)–(9) instead. The nonrelativistic polarization defined by Eqs. (1)–(3) should have the same feature as the relativistic one by Eqs. (4)–(9).

Throughout this paper, we use the coordinate system shown in Fig. 1, where two nuclei at ($x = \pm b/2,\ y = 0$) in the transverse plane move along the $\pm z$ direction, respectively, and the global OAM $\mathbf{J}$ is along the $-y$ direction. Due to the OAM of the fireball, a net vorticity field is expected to form whose direction is pointing to the OAM in average. In the following we formally denote such a net vorticity as $\langle\omega_y\rangle$, where $\langle\rangle$ means the average over space weighted by the matter density. This net vorticity leads to a global polarization $\mathbf{P}^G$ along the direction of the OAM.

Apart from the net vorticity originated from the OAM, vorticity can also be generated from the fireball's nonuniform expansion as illustrated by Fig. 2, whose pattern is very different from the net vorticity (along $-y$ direction). For simplicity, let us consider an isotropic transverse velocity field

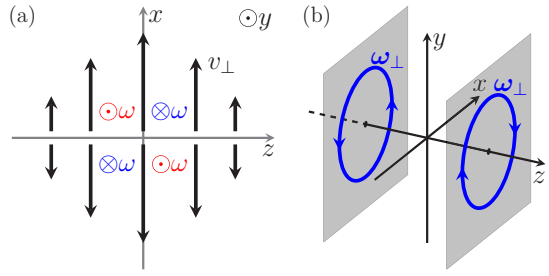

FIG. 2. (a) Schematic illustration of the quadrupole pattern of ω_y generated from $\partial_z v_\perp$ in the reaction plane, where the vorticity is along the $-y$ direction ($\otimes$) in the $xz > 0$ quadrants and the y direction ($\odot$) in the $xz < 0$ quadrants. (b) A three-dimensional view of the circular structure of the transverse vorticity $\boldsymbol{\omega}_\perp = (\omega_x, \omega_y)$.

$\mathbf{v}_\perp = (v_x, v_y)$ in the following form

$$\mathbf{v}_\perp = v_\perp(r,z)\mathbf{e}_r, \tag{10}$$

where r and z are the transverse radius and the longitudinal coordinate, and $\mathbf{e}_r$ is the unit vector along the radial direction in the transverse plane. Then from Eq. (1), the transverse vorticity filed $\boldsymbol{\omega}_\perp = (\omega_x, \omega_y)$ is given by

$$\boldsymbol{\omega}_\perp = \tfrac{1}{2}\partial_z v_\perp(r,z)\mathbf{e}_\phi, \tag{11}$$

where $\mathbf{e}_\phi = (-\sin\phi, \cos\phi, 0)$ is the unit vector along the azimuthal direction with ϕ being the azimuthal angle with respect to the x axis. If the fluid is the Bjorken-type with the longitudinal boost invariance that $v_\perp$ is independent of z, then $\boldsymbol{\omega}_\perp$ is zero. However, in realistic collisions the longitudinal boost invariance is violated since the matter is not uniformly distributed in space, which can give rise to a nonzero vorticity. Note that the energy or matter is mostly deposited at $z = 0$, the pressure-driven transverse velocity $v_\perp$ should be the largest at $z = 0$ and decrease with $|z|$ as shown in Fig. 2(a). Then with the gradients $\partial v_\perp/\partial|z| < 0$, one can see that $\boldsymbol{\omega}_\perp$ in Eq. (11) has a circular structure: $\boldsymbol{\omega}_\perp$ is along $-\mathbf{e}_\phi$ (clockwise) and $\mathbf{e}_\phi$ (counterclockwise) in the $z > 0$ and $z < 0$ regions respectively as shown in Fig. 2(b). In terms of the components ω_x and ω_y, they have the quadrupole structures: $\omega_x > 0$ ($\omega_x < 0$) in the $yz > 0$ ($yz < 0$) quadrants and $\omega_y > 0$ ($\omega_y < 0$) in the $xz < 0$ ($xz > 0$) quadrants.

We show the quadrupole or circular pattern of the transverse vorticity obtained in numerical calculations with the AMPT model in Figs. 3 and 4, which correspond to the illustrations in Figs. 2(a) and 2(b), respectively.

Figure 3 shows the y component of the vorticity in the $x\eta_s$ plane at $y = 0$, where $\eta_s = (1/2)\log[(t+z)/(t-z)]$ is the space-time rapidity. Here the vorticity field is shown at the time $t = 5$ fm/c in 20–30 % central Au+Au collisions at $\sqrt{s_{\rm NN}} =$ 7.7 and 200 GeV. We see that ω_y at 200 GeV has a nearly prefect quadrupole structure: ω_y is an odd function of both x and η_s. This pattern is consistent with what we expect in Fig. 2(a). As for 7.7 GeV, ω_y is not an odd function. In particular, we see that $\omega_y < 0$ in the central region $x \simeq \eta_s \simeq 0$. Such a deviation from the odd function comes from the fireball's tilted geometry in the reaction plane in noncentral collisions as shown in Fig. 1(b). We can regard the pattern of ω_y as a sum

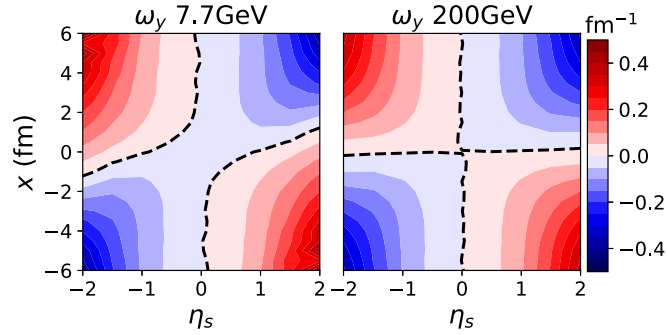

FIG. 3. The vorticity component ω_y in the reaction plane ($x\eta_s$ plane at $y = 0$) at time $t = 5$ fm/c in 20–30 % central Au+Au collisions at $\sqrt{s_{\rm NN}} = 7.7$ (left) and 200 GeV (right). The black dashed lines represent the contour where $\omega_y = 0$.

of two different vorticity patterns: the net vorticity generated from the fireball's tilted shape and the quadrupole one from the fireball's nonuniform expansion. The net vorticity pattern has an obvious energy dependence. At 200 GeV, the contribution from the net vorticity is very small since the fireball is less tilted in midrapidity at higher energy due to its faster longitudinal expansion [22,42]. In contrast the quadrupole vorticity has the same magnitude at 7.7 and 200 GeV. See Refs. [22,23,31–35] for other calculations of the quadrupole structure of ω_y.

Figure 4 shows the distribution of $\boldsymbol{\omega}_\perp = (\omega_x, \omega_y)$ as functions of x and y at two values of space-time rapidity $\eta_s = -1$ and 1. Here the vorticity field is shown at the time $t = 5$ fm/c in 20–30 % central Au+Au collisions at $\sqrt{s_{\rm NN}} = 200$ GeV for instance. We see that $\boldsymbol{\omega}_\perp$ has a circular structure with opposite orientations in the $\eta_s > 0$ and $\eta_s < 0$ regions. This pattern is consistent with what we expect in Fig. 2(b). The behavior that the magnitude of $\boldsymbol{\omega}_\perp$ increases with the transverse radius r can be understood by the increase of $v_\perp(r,z)$ with r. The circular pattern of $\boldsymbol{\omega}_\perp$ has also been observed in Ref. [27].

Besides the transverse component $\boldsymbol{\omega}_\perp$, the longitudinal component ω_z also has a nonvanishing local distribution. Due to the anisotropic flow, $\mathbf{v}_\perp$ in noncentral collisions is not along

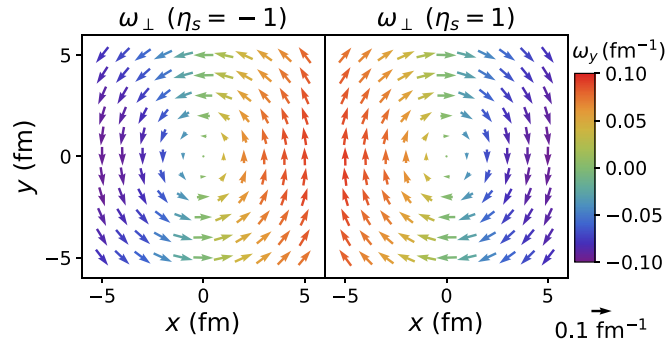

FIG. 4. The distribution of the transverse vorticity $\boldsymbol{\omega}_\perp = (\omega_x, \omega_y)$ in the transverse plane at longitudinal positions $\eta_s = -1$ (left) and $\eta_s = 1$ (right) at time $t = 5$ fm/c in 20–30 % central Au+Au collisions at $\sqrt{s_{\rm NN}} = 200$ GeV. The color represents the value of the component ω_y.

TABLE I. The sources and Λ polarization effects of different vorticity patterns.

Vorticity pattern	Source	Effect on Λ polarization
net vorticity $\langle\omega_y\rangle < 0$	global OAM or fireball's tilted shape	global polarization P_y^G
circular structure of $\boldsymbol{\omega}_\perp$	longitudinal dependence of transverse velocity	local polarization, see P_x and P_y in Eq. (12)
quadrupole structure of ω_z	anisotropic transverse velocity (elliptic flow)	local polarization, see P_z in Eq. (12)

the radial direction $\mathbf{e}_r$, this gives rise to the inequality of $\partial_x v_y$ and $\partial_y v_x$, and then a nonvanishing ω_z with the quadrupole pattern in the transverse plane: ω_z are along the opposite directions in the regions $\sin(2\phi) > 0$ and $\sin(2\phi) < 0$ [11,40].

In experiments, one can measure the local Λ polarization to probe the quadrupole or circular pattern of the vorticity field. Due to the collective expansion of the fireball, the space information of the vorticity field can be reflected by the local Λ polarization as functions of ϕ_p and Y, where ϕ_p is the azimuthal angle of Λ's momentum with respect to the reaction plane and $Y = (1/2)\log[(E_p + p_z)/(E_p - p_z)]$ is the momentum rapidity. From the circular structure of the transverse vorticity $\boldsymbol{\omega}_\perp$ in Eq. (11) and the quadrupole pattern of the longitudinal vorticity ω_z, to the leading order of the Fourier decomposition, we expect that the polarization vector $\mathbf{P} = (P_x, P_y, P_z)$ for the Λ hyperon has the following harmonic behavior:

$$\begin{aligned} P_x(\phi_p, Y) &= F_x \mathrm{sgn}(Y) \sin\phi_p, \\ P_y(\phi_p, Y) &= -F_y \mathrm{sgn}(Y) \cos\phi_p, \\ P_z(\phi_p, Y) &= -F_z \sin(2\phi_p), \end{aligned} \tag{12}$$

where F_x, F_y, and F_z are the Fourier coefficients, which are all positive, and $\mathrm{sgn}(Y)$ denotes the sign of Y coming from the opposite circular orientations of $\boldsymbol{\omega}_\perp$ at $\eta_s > 0$ and $\eta_s < 0$ as shown in Fig. 2(b) and Fig. 4.

In summary of this section, there are three different vorticity patterns as listed in Table I. They are the net vorticity $\langle\omega_y\rangle$ from the fireball's tilted shape in the reaction plane, the circular transverse vorticity $\boldsymbol{\omega}_\perp$ from the longitudinal dependence of the transverse velocity, and the quadrupole structure of ω_z from the anisotropic transverse velocity. These three vorticity patterns can lead to the global polarization P_y^G, the circular polarization (P_x, P_y) in the transverse directions and the local polarization P_z in the longitudinal direction, respectively. Since the three vorticity patterns are from different sources, their effects on Λ polarization could have different energy and centrality behaviors, which are studied in the next section.

IV. NUMERICAL RESULTS AND DISCUSSIONS

In this section, we show the numerical results of the local Λ polarization using the string-melting version of the AMPT model [43] as the event generator. In this model, the collision participants are converted to partons, which are allowed to interact by two-body elastic scatterings. In this partonic phase the collective flow velocity and vorticity are generated, and we calculate the thermal vorticity $\varpi_{\mu\nu}$ in Eq. (4) by the same coarse-grain method as in Ref. [22]. At the end of the partonic phase, the Λ hyperons are produced by a coalescence mechanism. Then their polarizations are calculated with Eqs. (7)–(9) with the values of $\varpi_{\mu\nu}$ at the space-time point at which the Λ hyperons are produced.

We run simulations of Au+Au collisions at energies $\sqrt{s_{\mathrm{NN}}} = 7.7$, 11.5, 14.5, 19.6, 27, 39, 62.4, 200 GeV and also Pb+Pb collisions at 2760 GeV. For each collision energy, 5×10^5 events are generated with varying impact parameter b limited to the range 0–25 fm. These events are classified into different centrality bins 0–10 %, 10–20 %, ... according to the charged particle multiplicities. For each collision energy and

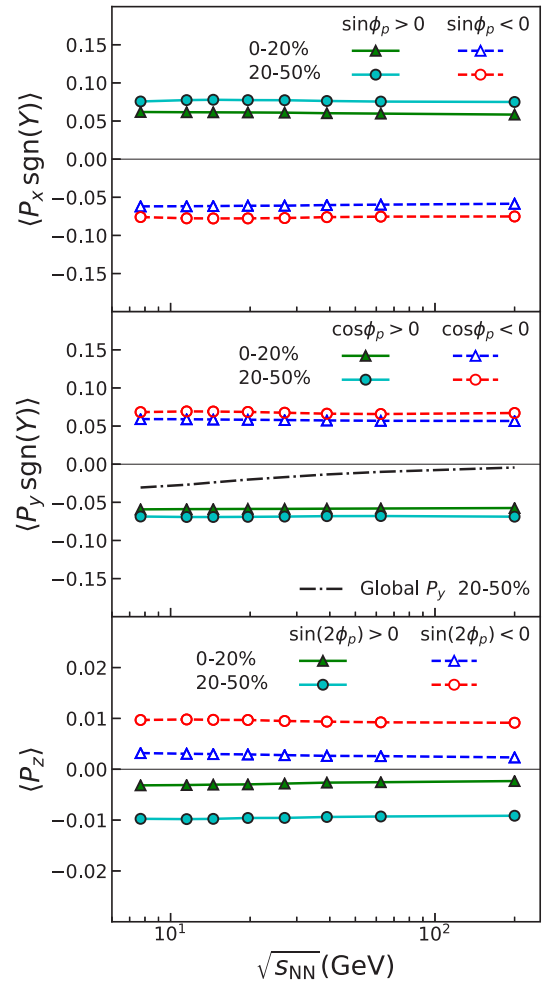

FIG. 5. The average polarizations $\langle P_x \mathrm{sgn}(Y)\rangle$, $\langle P_y \mathrm{sgn}(Y)\rangle$, and $\langle P_z\rangle$ for the Λ hyperons with different signs of $\sin\phi_p$, $\cos\phi_p$, and $\sin(2\phi_p)$ as functions of collision energies in the range 7.7–200 GeV in 0–20 % (triangle) and 20–50 % (circle) central Au+Au collisions. The black dot-dashed line shown in the middle panel refers to the global polarization of Λ hyperons in the centrality bin 20–50 % in midrapidity region $|Y| < 1$.

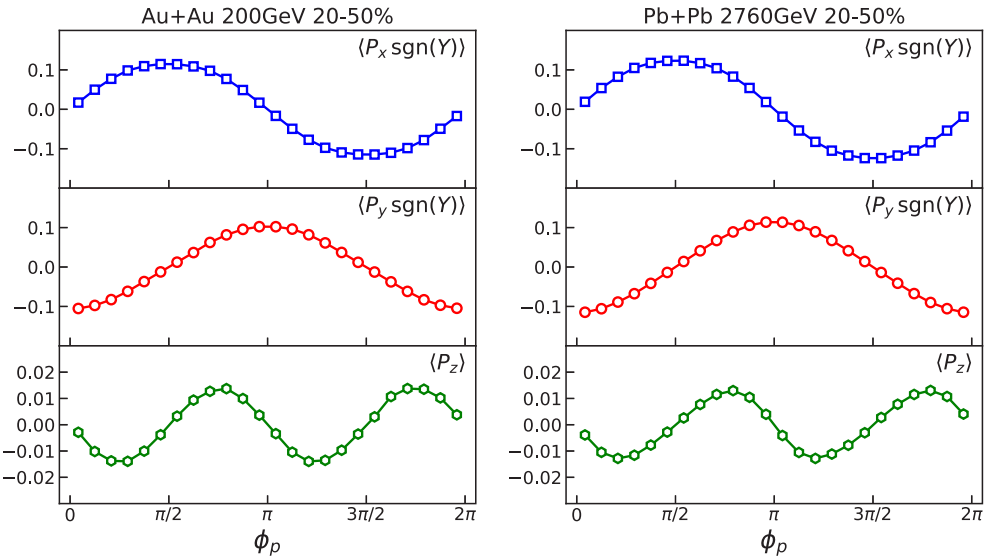

FIG. 6. The average polarizations $\langle P_x \mathrm{sgn}(Y)\rangle$, $\langle P_y \mathrm{sgn}(Y)\rangle$, and $\langle P_z\rangle$ for Λ as functions of azimuthal angle ϕ_p in 20–50 % central Au+Au collisions at 200 GeV (left) and Pb+Pb collisions at 2760 GeV (right).

centrality, we calculate the polarizations of all the Λ hyperons in the rapidity region $|Y| < 1$.

To probe the vorticity structure, we group all Λ hyperons into several bins by their azimuthal angle ϕ_p and the sign of Y. Then we calculate the average of the polarization vector for Λ in each bin. The result $\mathbf{P}(\phi_p, Y)$ is obtained as a function of ϕ_p and Y. To test Eq. (12), we define the following quantities:

$$\langle P_x \mathrm{sgn}(Y)\rangle = \frac{P_x(\phi_p, Y>0) - P_x(\phi_p, Y<0)}{2},$$
$$\langle P_y \mathrm{sgn}(Y)\rangle = \frac{P_y(\phi_p, Y>0) - P_y(\phi_p, Y<0)}{2},$$
$$\langle P_z\rangle = \frac{P_z(\phi_p, Y>0) + P_z(\phi_p, Y<0)}{2}. \quad (13)$$

Here the averages in the first two lines are taken with weight $\mathrm{sgn}(Y)$. In this way, the global polarization $\mathbf{P}^G$ along $-y$ direction in both $Y > 0$ and $Y < 0$ region is removed, but the circular polarizations P_x and P_y in Eq. (12) survive. Then using Eq. (13), we can focus on the effects from the circular or quadrupole patterns of the local vorticity. Note that the three quantities in Eq. (13) are functions of ϕ_p only.

Figure 5 shows the results of $\langle P_x \mathrm{sgn}(Y)\rangle$, $\langle P_y \mathrm{sgn}(Y)\rangle$, and $\langle P_z\rangle$ for the Λ hyperons in different regions of ϕ_p as functions of collision energies in the range 7.7–200 GeV in 0–20 % and 20–50 % central Au+Au collisions. Here the azimuthal angle is divided into different regions by the signs of $\sin\phi_p$, $\cos\phi_p$, and $\sin(2\phi_p)$ for the calculations of P_x, P_y, and P_z, respectively. We can see that $\langle P_x \mathrm{sgn}(Y)\rangle$ is positive (negative) in region $\sin\phi_p > 0$ (<0) and $\langle P_y \mathrm{sgn}(Y)\rangle$ is negative (positive) in region $\cos\phi_p > 0$ (<0), which are consistent with the circular structure of the transverse vorticity. Also we see $\langle P_z\rangle$ is negative (positive) in region $\sin(2\phi_p) > 0$ (<0), which is also consistent with the quadrupole pattern of ω_z in the transverse plane.

For comparison, we also show the global polarization $\mathbf{P}^G$ of Λ by the black dot-dashed line in the middle panel of Fig. 5. The global polarization $\mathbf{P}^G$ is the effect from the net vorticity $\langle\omega_y\rangle$. It is calculated by taking an average over all Λ hyperons without dividing them into bins by ϕ_p and Y. From the reflection symmetry of the fireball, one can prove that only the P_y^G component (along the OAM) is nonvanishing. As discussed in Sec. III, the global polarization P_y^G and the net vorticity $\langle\omega_y\rangle$ are originated from the fireball's tilted shape in the reaction plane. Since the fireball is less tilted in midrapidity at higher energies, the global polarization P_y^G decreases with the collision energy. However, the circular polarization observables $\langle P_x \mathrm{sgn}(Y)\rangle$ and $\langle P_y \mathrm{sgn}(Y)\rangle$ are not sensitive to the collision energy, which is due to that the circular vorticity pattern has the same magnitude at different collision energies as evidenced in Fig. 3. The local polarization effect along the longitudinal direction $\langle P_z\rangle$ also has a flat energy behavior. This may be related to that hadron's elliptic flow does not significantly change with the collision energy [44].

Figure 6 shows the results of $\langle P_x \mathrm{sgn}(Y)\rangle$, $\langle P_y \mathrm{sgn}(Y)\rangle$, and $\langle P_z\rangle$ for the Λ hyperons as functions of azimuthal angle ϕ_p in 20–50 % central Au+Au collisions at 200 GeV and Pb+Pb collisions at 2760 GeV, where the whole range of ϕ_p is divided into 24 bins. We can see that the shapes of $\langle P_x \mathrm{sgn}(Y)\rangle$, $\langle P_y \mathrm{sgn}(Y)\rangle$, and $\langle P_z\rangle$ are in analogy to $\sin\phi_p$, $-\cos\phi_p$, and $-\sin(2\phi_p)$, respectively, as described by Eq. (12). The features of three quantities at two collision energies are quite similar. We have also checked that the harmonic behaviors also exist at energies 7.7–62.4 GeV. We note that our result for $\langle P_z\rangle$ is consistent with the viscous hydrodynamic simulations [40], while $\langle P_x \mathrm{sgn}(Y)\rangle$ and $\langle P_y \mathrm{sgn}(Y)\rangle$ are not calculated in that reference. It is worthwhile to point out that although the global polarization components P_x^G and P_z^G are zero due to the symmetry and P_y^G is almost vanishing at $\sqrt{s_{\mathrm{NN}}} = 200$ GeV [45] and 2760 GeV [46] due to the reason given in the above paragraph, the local polarization observables $\langle P_x \mathrm{sgn}Y\rangle$, $\langle P_y \mathrm{sgn}Y\rangle$, and $\langle P_z\rangle$ are all nonvanishing. We also see in Fig. 5 that the magnitude of $\langle P_y \mathrm{sgn}Y\rangle$ is larger than that of P_y^G. Therefore the local polarization effects are sizable and worthy to be tested in future experiments.

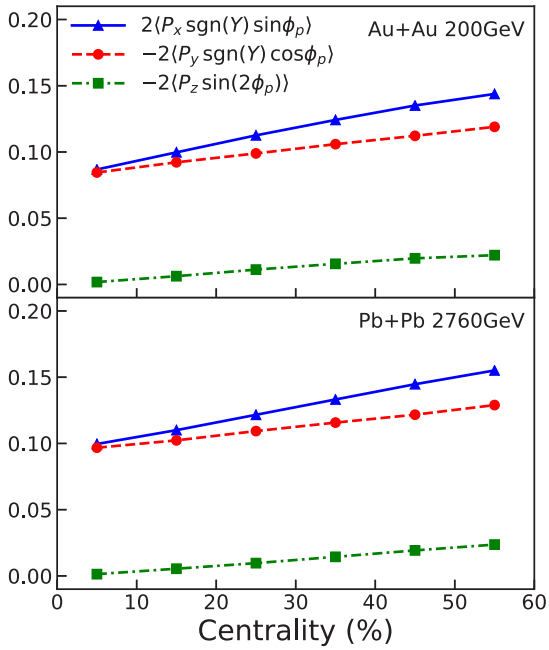

FIG. 7. The Fourier coefficients in Eq. (14) as functions of the centrality at 200 GeV for Au+Au collisions (top) and 2760 GeV for Pb+Pb collisions (bottom).

The Fourier coefficients F_x, F_y, and F_z in Eq. (12) can be extracted from the magnitude of the harmonic behavior in Fig. 6,

$$\begin{aligned} F_x &= 2\langle P_x \mathrm{sgn}(Y)\sin\phi_p\rangle, \\ F_y &= -2\langle P_y \mathrm{sgn}(Y)\cos\phi_p\rangle, \\ F_z &= -2\langle P_z \sin(2\phi_p)\rangle, \end{aligned} \tag{14}$$

where the averages are taken over 24 bins of the azimuthal angle. The results are shown in Fig. 7 as functions of the centrality at $\sqrt{s_{\mathrm{NN}}} = 200$ GeV for Au+Au and at 2760 GeV for Pb+Pb collisions. The features of these coefficients are quite similar at two energies. We see that F_x and F_y are at the same magnitude, but there is a difference between them, which increases with the centrality. This is because the transverse vorticity loop in noncentral collisions should be in an elliptic shape, which deviates from a prefect circle. We also see that in the most central collisions F_x and F_y are nonvanishing, while F_z is almost zero. This difference can be understood by the fact that F_z arises from the elliptic flow, which does not exist in central collisions while F_x and F_y are generated from the violation of the longitudinal boost invariance, which exists in both central and noncentral collisions.

V. SUMMARY

We give a systematic analysis on the vorticity structure and the distribution of Λ polarization in heavy-ion collisions. We find that there are two contributions to the vorticity field: one is from the OAM along the $-y$ direction giving the global polarization; another is from the nonuniform expansion of the fireball, which leads to a circular structure for the transverse vorticity $\boldsymbol{\omega}_\perp$ and a quadrupole pattern for the longitudinal vorticity ω_z in the transverse plane. The space distribution of the vorticity field can be probed by the local Λ polarization as a function of the azimuthal angle ϕ_p and the rapidity Y in momentum space, which is expected to have harmonic behaviors as in Eq. (12).

For the numerical calculation of the local Λ polarization, we use the string-melting version of the AMPT model. We run the simulations of Au+Au collisions at energies $\sqrt{s_{\mathrm{NN}}} =$ 7.7–200 GeV and Pb+Pb collisions at 2760 GeV. We divide all Λ hyperons into several bins by their azimuthal angle ϕ_p and the sign of Y. Then we calculate the average of the polarization vector for Λ in each bin. The results show that $\langle P_x \mathrm{sgn}(Y)\rangle$, $\langle P_y \mathrm{sgn}(Y)\rangle$, and $\langle P_z\rangle$ have the harmonic behaviors of $\sin\phi_p$, $-\cos\phi_p$, and $-\sin(2\phi_p)$, respectively, which are consistent to the circular or quadrupole structure of the vorticity field as we expect from the nonuniform collective expansion of the fireball. These patterns in the local Λ polarization are expected to be tested in future experiments.

ACKNOWLEDGMENTS

The authors thank Ai-hong Tang and Zhang-bu Xu for insightful discussions. The authors are supported in part by the Major State Basic Research Development Program (973 Program) in China under Grants No. 2015CB856902 and No. 2014CB845402 and by the National Natural Science Foundation of China (NSFC) under Grants No. 11535012 and No. 11720101001.

[1] Z.-T. Liang and X.-N. Wang, Phys. Rev. Lett. **94**, 102301 (2005); **96**, 039901(E) (2006).
[2] Z.-T. Liang and X.-N. Wang, Phys. Lett. B **629**, 20 (2005).
[3] J.-H. Gao, S.-W. Chen, W.-t. Deng, Z.-T. Liang, Q. Wang, and X.-N. Wang, Phys. Rev. C **77**, 044902 (2008).
[4] S.-w. Chen, J. Deng, J.-h. Gao, and Q. Wang, Front. Phys. China **4**, 509 (2009).
[5] X.-G. Huang, P. Huovinen, and X.-N. Wang, Phys. Rev. C **84**, 054910 (2011).
[6] F. Becattini and F. Piccinini, Ann. Phys. (N.Y.) **323**, 2452 (2008).
[7] F. Becattini, V. Chandra, L. Del Zanna, and E. Grossi, Ann. Phys. (N.Y.) **338**, 32 (2013).
[8] F. Becattini, I. Karpenko, M. A. Lisa, I. Upsal, and S. A. Voloshin, Phys. Rev. C **95**, 054902 (2017).
[9] R.-h. Fang, L.-g. Pang, Q. Wang, and X.-n. Wang, Phys. Rev. C **94**, 024904 (2016).
[10] Q. Wang, Nucl. Phys. A **967**, 225 (2017).
[11] S. A. Voloshin, EPJ Web Conf. **171**, 07002 (2018).
[12] F. Becattini, EPJ Web Conf. **171**, 07001 (2018).
[13] D. T. Son and P. Surowka, Phys. Rev. Lett. **103**, 191601 (2009).
[14] Y. Jiang, X.-G. Huang, and J. Liao, Phys. Rev. D **92**, 071501 (2015).

[15] H.-L. Chen, K. Fukushima, X.-G. Huang, and K. Mameda, Phys. Rev. D **93**, 104052 (2016).
[16] M. N. Chernodub and S. Gongyo, J. High Energy Phys. 01 (2017) 136.
[17] X.-G. Huang, K. Nishimura, and N. Yamamoto, J. High Energy Phys. 02 (2018) 069.
[18] Y. Jiang and J. Liao, Phys. Rev. Lett. **117**, 192302 (2016).
[19] L. Adamczyk *et al.* (STAR Collaboration), Nature (London) **548**, 62 (2017).
[20] I. Karpenko and F. Becattini, Eur. Phys. J. C **77**, 213 (2017).
[21] Y. Xie, D. Wang, and L. P. Csernai, Phys. Rev. C **95**, 031901 (2017).
[22] H. Li, L.-G. Pang, Q. Wang, and X.-L. Xia, Phys. Rev. C **96**, 054908 (2017).
[23] S. Shi, K. Li, and J. Liao, arXiv:1712.00878 [nucl-th].
[24] Y. Sun and C. M. Ko, Phys. Rev. C **96**, 024906 (2017).
[25] M. Baznat, K. Gudima, A. Sorin, and O. Teryaev, Phys. Rev. C **97**, 041902 (2018).
[26] M. Baznat, K. Gudima, A. Sorin, and O. Teryaev, Phys. Rev. C **88**, 061901 (2013).
[27] M. I. Baznat, K. K. Gudima, A. S. Sorin, and O. V. Teryaev, Phys. Rev. C **93**, 031902 (2016).
[28] L. P. Csernai, V. K. Magas, and D. J. Wang, Phys. Rev. C **87**, 034906 (2013).
[29] L. P. Csernai, D. J. Wang, M. Bleicher, and H. Stöcker, Phys. Rev. C **90**, 021904(R) (2014).
[30] F. Becattini, L. P. Csernai, and D. J. Wang, Phys. Rev. C **88**, 034905 (2013); **93**, 069901(E) (2016).
[31] F. Becattini, G. Inghirami, V. Rolando, A. Beraudo, L. Del Zanna, A. De Pace, M. Nardi, G. Pagliara, and V. Chandra, Eur. Phys. J. C **75**, 406 (2015); **78**, 354(E) (2018).
[32] O. Teryaev and R. Usubov, Phys. Rev. C **92**, 014906 (2015).
[33] Y. Jiang, Z.-W. Lin, and J. Liao, Phys. Rev. C **94**, 044910 (2016); **95**, 049904(E) (2017).
[34] Yu. B. Ivanov and A. A. Soldatov, Phys. Rev. C **95**, 054915 (2017).
[35] Y. B. Ivanov and A. A. Soldatov, Phys. Rev. C **97**, 044915 (2018).
[36] W.-T. Deng and X.-G. Huang, Phys. Rev. C **93**, 064907 (2016).
[37] L.-G. Pang, H. Petersen, Q. Wang, and X.-N. Wang, Phys. Rev. Lett. **117**, 192301 (2016).
[38] Y. L. Xie, M. Bleicher, H. Stöcker, D. J. Wang, and L. P. Csernai, Phys. Rev. C **94**, 054907 (2016).
[39] E. E. Kolomeitsev, V. D. Toneev, and V. Voronyuk, Phys. Rev. C **97**, 064902 (2018).
[40] F. Becattini and I. Karpenko, Phys. Rev. Lett. **120**, 012302 (2018).
[41] I. Karpenko and F. Becattini, EPJ Web Conf. **171**, 17001 (2018).
[42] X.-L. Xia, H. Li, and Q. Wang, PoS **311**, 023 (2018).
[43] Z.-W. Lin, C. M. Ko, B.-A. Li, B. Zhang, and S. Pal, Phys. Rev. C **72**, 064901 (2005).
[44] L. Adamczyk *et al.* (STAR Collaboration), Phys. Rev. C **93**, 014907 (2016).
[45] J. Adam *et al.* (STAR Collaboration), Phys. Rev. C **98**, 014910 (2018).
[46] A. Timmins (ALICE Collaboration), Nucl. Phys. A **967**, 43 (2017).